Experimental studies of direct-drive, low-intensity, low-adiabat spherical implosions on OMEGA

V. A. Smalyuk, R. Betti,[a] J. A. Delettrez, V. Yu. Glebov, V. N. Goncharov,[b] D. Y. Li, D. D. Meyerhofer, S. P. Regan, S. Roberts, T. C. Sangster, C. Stoeckl, and W. Seka
Laboratory for Laser Energetics, University of Rochester, 250 East River Road, Rochester, New York 14623-1299

J. A. Frenje, C. K. Li, R. D. Petrasso,[c] and F. H. Séguin
Plasma Science and Fusion Center, Massachusetts Institute of Technology, Cambridge, Massachusetts 02139

(Received 14 December 2006; accepted 4 January 2007; published online 6 February 2007)

Low-adiabat (high-compressibility) implosions were performed with ~860 μm diam, 24- and 35-μm-thick shells filled with 15 atm of D_2 gas driven with ~12.5 kJ, 3-ns-square pulse shapes, and a laser intensity of $\sim 2\times 10^{14}$ W/cm^2. Initial target modulations, imprinted on the target surface by laser nonuniformities, were varied by using drive with and without smoothing by spectral dispersion. The performance of the spherical implosions (with a gas fuel convergence of ~16) was correlated with measured target modulations at the end of the acceleration phase performed in a planar target with similar conditions using through-foil radiography. The neutron yield decreases sharply when target modulations become comparable with the target thickness at the end of the acceleration phase. The measured target areal densities are less sensitive to target modulations. Implosions with 35-μm-thick shells produced neutron-averaged areal densities that are among the highest on OMEGA [T. R. Boehly *et al.*, Opt. Commun. **133**, 495 (1997)]. © *2007 American Institute of Physics*. [DOI: 10.1063/1.2436752]

I. INTRODUCTION

The goal of inertial confinement fusion (ICF)[1,2] is to implode a spherical target to achieve fuel densities and temperatures adequate to sustain thermonuclear burn. Rayleigh–Taylor (RT)[3,4] instability is of critical importance in ICF because it leads to shell disruption and performance degradation.[2] A direct-drive implosion begins with an acceleration phase when the laser beams ablate the shell surface and the capsule starts to converge. At this stage, outer-shell nonuniformities grow due to the acceleration-phase RT instability.[5–10] As the shell accelerates, the front-surface perturbations feed through the shell, seeding perturbations on the inner surface. When the laser is turned off, the ablation front becomes stable and the shell starts to decelerate while continuing to converge. During the deceleration phase, the inner surface modulations of the shell grow due to deceleration-phase RT instability[11] and Bell–Plesset (BP) convergent effects.[12]

The direct-drive experimental program on the OMEGA laser uses plastic and cryogenic D_2 and deuterium-tritium (DT) implosions to understand various aspects of ICF physics, including the equation of state of hot and dense matter, local and nonlocal electron transport, radiation transport, and the effects of hydrodynamic instabilities. Measuring the performance of both high- and low-adiabat implosions is important to test hydrocode predictions, utilizing the same code used in the direct-drive ignition design on the National Ignition Facility (NIF). The adiabat α is defined as the ratio of the fuel pressure to the Fermi-degenerate pressure at any particular density and is minimized by minimizing the fuel temperature. The low-temperature fuel is at a lower adiabat, and it can be more effectively compressed with a higher fuel ρR achieved than the higher-temperature fuel. Recent direct-drive implosions[13,14] on OMEGA (both high and low adiabat) used a laser drive at a maximum intensity of $\sim 1\times 10^{15}$ W/cm^2 (the same as in the direct-drive ignition design). The low-adiabat (α=2.4) implosions presented in this article were performed at a lower intensity of $\sim 2\times 10^{14}$ W/cm^2. These implosions were designed to be at a low intensity to avoid complications of nonlocal heat transport present at high intensities.[15] In these experiments the spherical implosions were complemented with planar-target experiments to measure modulation growth using backlighter x rays with through-foil radiography. The performance of the spherical implosions was correlated with measured planar-target modulation levels at the end of the acceleration phase. These measurements provide a direct relation between modulation levels produced by RT instability and spherical target performance.

Section II describes spherical experiments. Section III describes planar-target results. A discussion of experimental results and their relationship to simulations is in Sec. IV, and the conclusions are presented in Sec. V.

II. SPHERICAL-IMPLOSION RESULTS

Figure 1 shows a schematic of spherical targets [Fig. 1(a)] and the pulse shape used in the experiments [Fig. 1(b)].

[a]Also at Departments of Mechanical Engineering and Physics and Astronomy at University of Rochester.
[b]Also at Department of Mechanical Engineering at University of Rochester.
[c]Also at Laboratory for Laser Energetics.

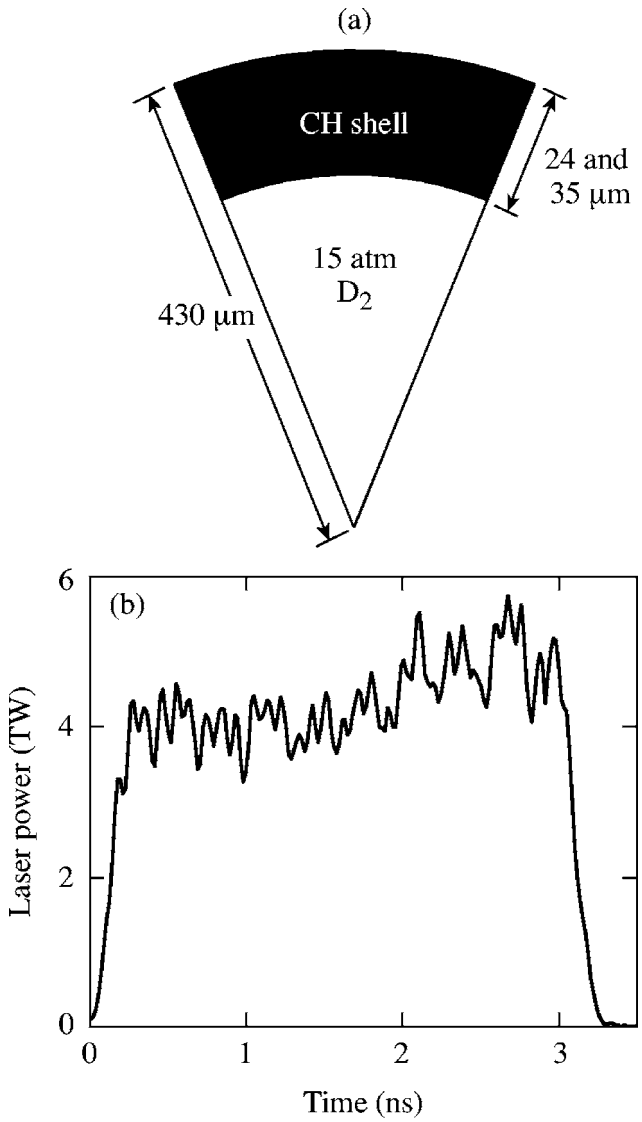

FIG. 1. (a) Schematic of the targets with ~430-μm initial radii, 24- and 35-μm-thick shells, filled with 15 atm of D_2 gas. (b) A 3-ns-square pulse shape at a total laser energy of ~12.5 kJ and an intensity of ~2×10^{14} W/cm^2.

The targets having ~430 μm initial radii, 24- and 35-μm-thick CH shells, and filled with 15 atm of D_2 gas, were imploded by 351 nm laser light using the 60-beam OMEGA laser system[16] with a 3-ns-square pulse shape at a total energy of ~12.5 kJ and a laser intensity of ~2×10^{14} W/cm^2. All shots were taken with laser beams smoothed by distributed phase plates (DPPs)[17] and polarization smoothing (PS)[18] using birefringent wedges. To vary initial modulation levels, the implosions were performed with and without 1 THz, two-dimensional smoothing by spectral dispersion (2D SSD).[19] The average beam-to-beam energy imbalance was ~3%. The predicted implosion performance was calculated by the one-dimensional (1D) hydrocode LILAC.[20] Figure 2 shows the measured absorption fraction as a function of the 1D calculated absorption fraction. Implosions with 35-μm-thick shells have a little higher absorption than implosions with 24-μm-thick shells because thicker shells move shorter distances in the acceleration phase, resulting in less laser light

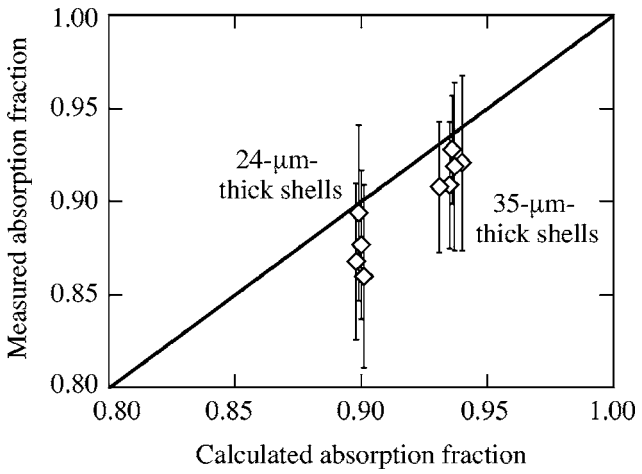

FIG. 2. Measured absorption fraction as a function of the 1D calculated absorption fraction.

missing the target. The calculated laser absorption is in very good agreement with that which is measured. Figure 3 shows four examples of measured (dashed curves) and calculated (solid curves) neutron-production histories for shots with 24-μm-thick shells [Figs. 3(a) and 3(c)] and with 35-μm-thick shells [Figs. 3(b) and 3(d)]. Data with SSD are shown in Figs. 3(a) and 3(b), while data without SSD are shown in Figs. 3(c) and 3(d). This, together with absorption data in Fig. 2, shows that LILAC's laser-coupling predictions are very good for these conditions.

Figure 4 shows measured neutron results and their comparison with LILAC predictions. Implosions with SSD have higher neutron yields than the implosions without SSD for both 24-μm- and 35-μm-thick shells, as shown in Fig. 4(a). The measured ion temperatures are also higher in implosions with SSD [see Fig. 4(b)]. The ratios of measured and calcu-

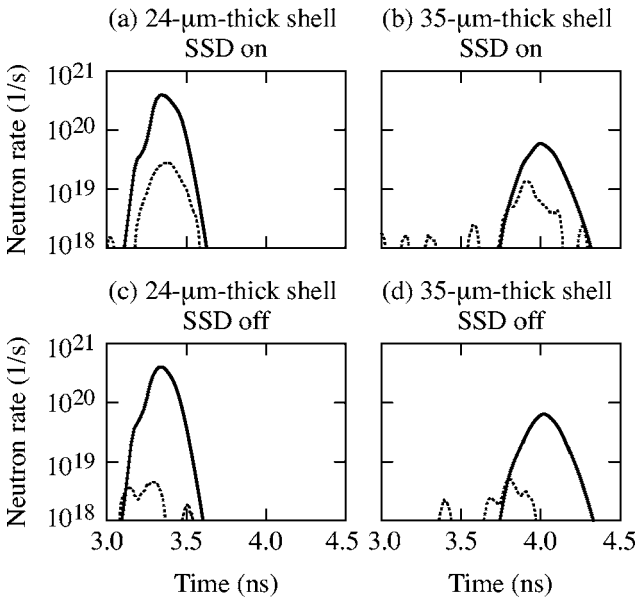

FIG. 3. Examples of measured (dashed curves) and calculated (solid curves) neutron-production histories for shots with 24-μm-thick shells [(a) and (c)] and with 35-μm-thick shells [(b) and (d)]. Data with SSD are shown in (a) and (b), while data without SSD are shown in (c) and (d).

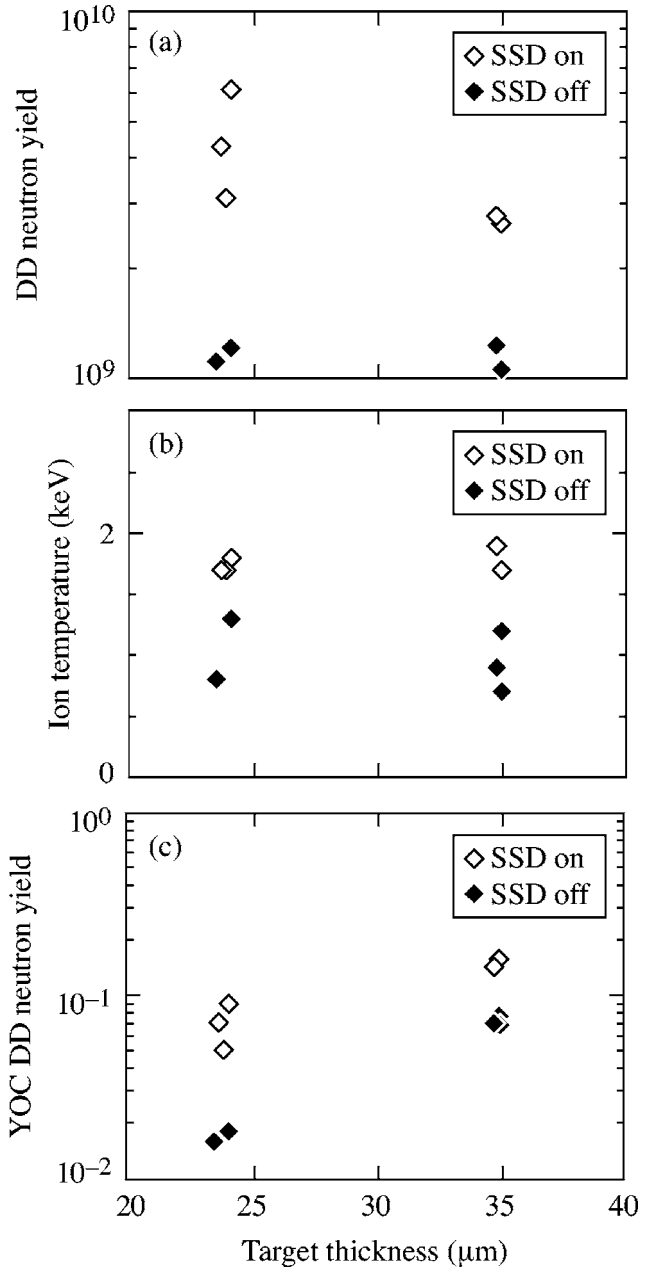

FIG. 4. (a) Measured neutron yields, (b) ion temperatures, and (c) neutron yields over clean (YOCs) as a function of shell thickness.

lated (or "clean") neutron yields (called yield over clean, or YOC) are shown in Fig. 4(c). The neutron-yield performance of the implosions with SSD is a factor of 3–5 better than in the implosions without SSD. At the same time, implosions with thicker, 35-μm-thick shells have higher YOCs than implosions with thinner, 24-μm-thick shells. Figure 5 shows measured secondary D^3He proton spectra for all four experimental conditions and inferred neutron-averaged areal densities (or ρRs).

These spectra were averaged over 2–3 shots per condition and over three detectors used in each shot. In implosions with 35-μm-thick shells, the measured neutron-averaged areal densities are among the highest measured so far in OMEGA direct-drive implosions. The measured peak ρRs for both 24-μm- and 35-μm-thick shells with SSD on (esti-

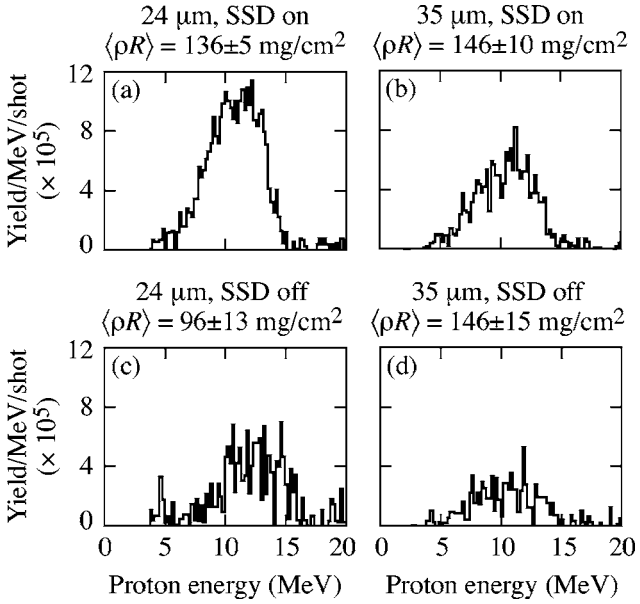

FIG. 5. Measured secondary proton spectra for (a) a 24-μm-thick shell with SSD on; (b) a 35-μm-thick shell with SSD on; (c) a 24-μm-thick shell with SSD off; and (d) a 35-μm-thick shell with SSD off.

mated from the end points of measured secondary proton spectra including effects of ion-temperature and geometrical broadenings) are about ~180 mg/cm^2. These measurements are compared with LILAC simulations discussed in Sec. IV.

Figure 6(a) shows x-ray images measured with a framing camera around peak compression for the shot taken with a 24-μm-thick shell with SSD. The temporal resolution of these images is ~40 ps, while the spatial resolution is ~10 μm. Shorter-scale modulations in these images evolve into longer-scale modulations as the target passes through peak compression and enters a rebound stage. This is typical behavior for the modulations as they grow due to deceleration-phase RT instability around peak compression (see Ref. 11 for a more detailed study of deceleration-phase modulation growth). Figure 6(b) compares peak-compression core images for all four conditions studied in

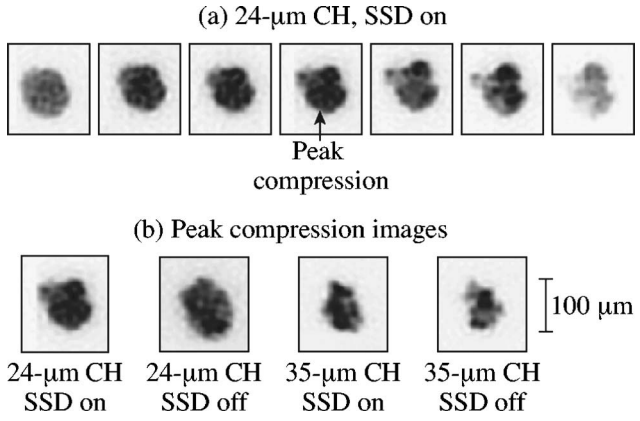

FIG. 6. (a) X-ray images measured with a framing camera around peak compression for the shot taken with a 24-μm-thick shell with SSD. The temporal distance between the images is ~60 ps. (b) Peak-compression core images for all four conditions studied in the experiments.

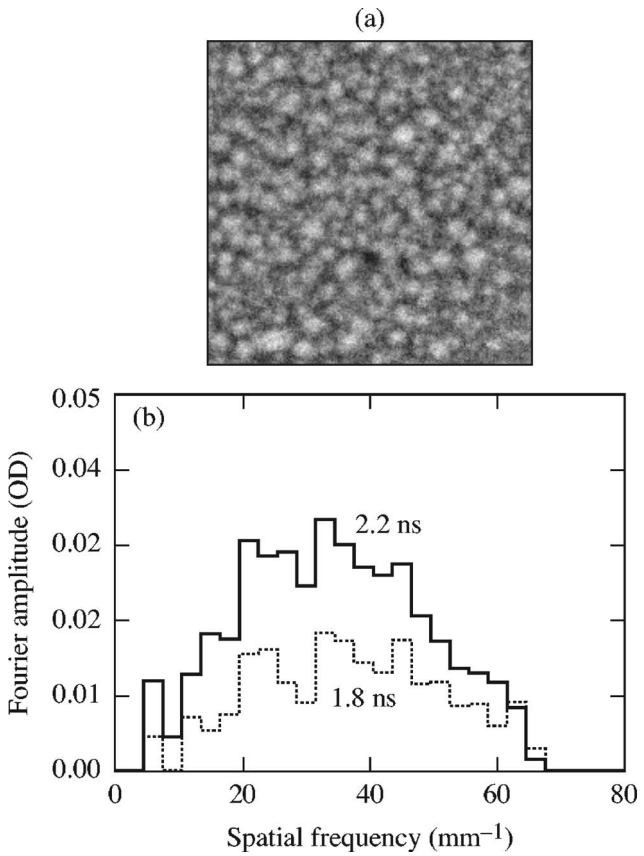

FIG. 7. Examples of (a) an optical-depth (OD) image measured at 2.2 ns and (b) modulation spectra measured at 1.8 ns and 2.2 ns in the experiment with a 24-μm-thick target without SSD.

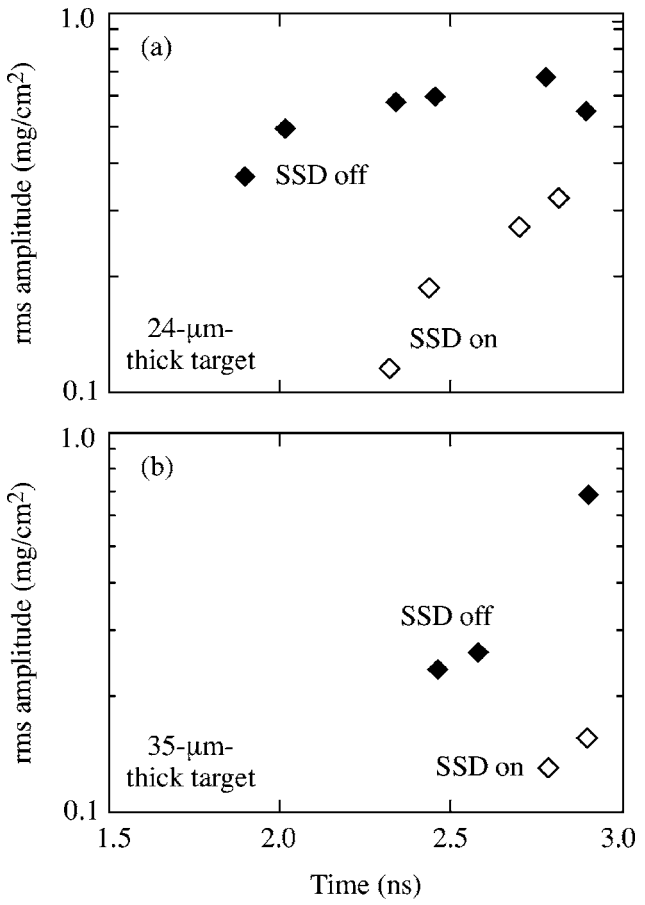

FIG. 8. The evolution of modulations measured in (a) 24-μm-thick targets and (b) in 35-μm-thick targets with SSD (open diamonds) and without SSD (closed diamonds).

these experiments. The images with 24-μm-thick shells are larger than with 35-μm-thick shells, indicating more compression in thicker-shell implosions (this is consistent with areal-density data shown in Fig. 5). The modulations levels in all these images are significantly higher than in other high-intensity, low-adiabat, and high-adiabat implosions,[13,14] indicating that these implosions are more unstable.

The performance of more stable implosions (with thicker shells and with SSD) is better than that of more unstable implosions (with thinner shells and without SSD). To quantify this, the experiments with planar targets were used to determine modulation levels (driven by RT instability) at the end of the acceleration phase and to correlate these modulation levels with implosion performances.

III. PLANAR-TARGET EXPERIMENTS

To complement spherical experiments, planar-target experiments[11] were performed in which modulation levels were measured at the end of the acceleration phase. In the planar experiments, initially smooth 1-mm-diam CH targets, with thicknesses of 20 and 35 μm, were driven with 3-ns-square pulses at a laser intensity of $\sim 2\times 10^{14}$ W/cm^2 using 11 OMEGA laser beams.[11] As in the spherical experiments, beam-smoothing techniques included DPPs, SSD, and PS. The modulation growth was measured with through-foil, x-ray radiography.[11] The backlighter x rays that probe target modulations were imaged by an 8-μm pinhole array onto a framing camera, allowing up to eight images with a temporal resolution of $\sim$80 ps and a spatial resolution of $\sim$10 μm to be captured at different times in each shot.

The typical optical-depth (OD) image of an x-ray radiograph is shown in Fig. 7(a) for an experiment with a 24-μm-thick target taken without SSD at 2.2 ns. Figure 7(b) shows examples of modulation spectra measured at 1.8 and 2.2 ns in that experiment. Figure 8 shows the evolution of modulations measured in 24-μm-thick targets [Fig. 8(a)] and in 35-μm-thick targets [Fig. 8(b)] showing data taken with SSD (open diamonds) and without SSD (closed diamonds). In the experiments with 24-μm-thick targets, the modulations in a shot without SSD grow less rapidly than in a shot with SSD. This is because the amplitude of these modulations is comparable with the target thickness (the target areal density is $\sim$1 mg/cm^2 and is comparable to the modulation level at the end of the drive, $\sim$0.5 mg/cm^2). At this point the target does not have enough thickness to support further RT growth. Modulations in 35-μm-thick targets continue to grow without slowing down even at the end of the drive, because the targets are thicker (the target areal density is $\sim$2.4 mg/cm^2 at $\sim$3 ns).

IV. DISCUSSION

Figure 9(a) shows a comparison of the implosion performance of 35-μm-thick targets (diamonds connected by a solid line) and 24-μm-thick targets (diamonds connected by

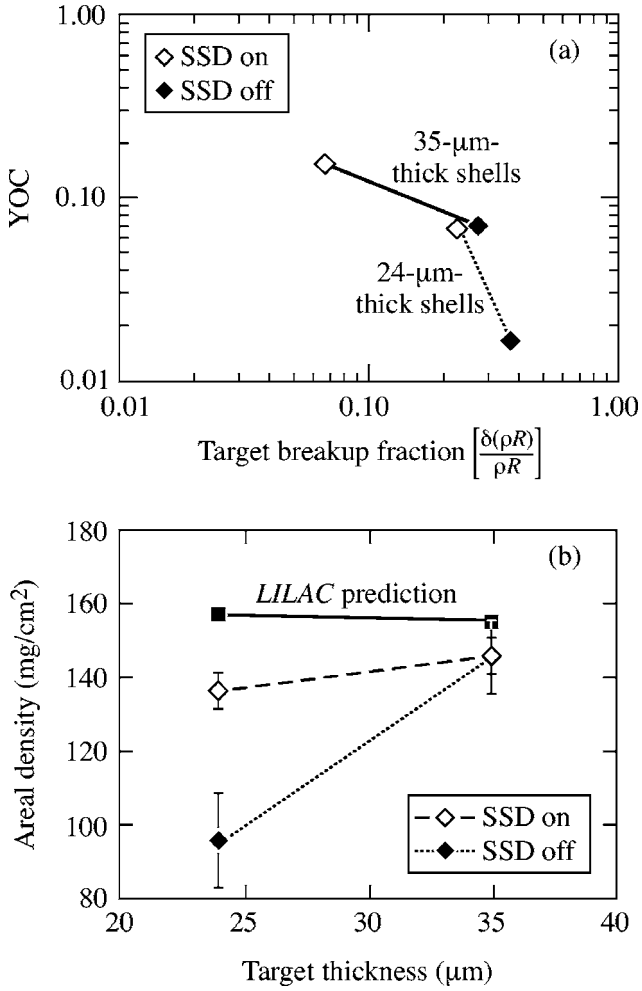

FIG. 9. (a) Comparison of the YOCs of 35-μm-thick targets (diamonds connected by a solid line) and 24-μm-thick targets (diamonds connected by a dashed line) as a function of the measured (in planar targets) target-breakup fraction at the end of the acceleration phase. (b) Comparison of measured and calculated neutron-averaged areal ρRs. Measured areal densities with SSD are shown by diamonds. LILAC predictions are shown by squares.

a dashed line). The YOC data were averaged over all data taken at their corresponding conditions. The target-breakup fraction was calculated using planar-target, areal-density modulation levels measured at the end of the drive normalized to the calculated target areal density at the end of the drive. The neutron YOC decreases sharply when the target-breakup fraction becomes larger than ~0.2–0.3 at the end of the acceleration phase. Figure 9(b) shows a comparison of measured and calculated neutron-averaged areal densities (or ρRs). In implosions with 35-μm-thick shells, the measured areal densities with SSD (triangles) and without SSD (squares) are close to their LILAC predictions (diamonds), while in more unstable implosions, with 24-μm-thick shells, the measured areal densities are lower than their predictions. There is a little degradation of target areal density when the shell integrity is less than ~0.2–0.3. The measured target areal densities are less sensitive to target modulations than YOCs.

V. CONCLUSIONS

Low-adiabat ($\alpha \sim 2.4$) implosions were performed with 24- and 35-μm-thick shells filled with 15 atm of D_2 gas and driven with 3-ns-square pulse shapes at a laser intensity of $\sim 2 \times 10^{14}$ W/cm^2. Initial target modulations, imprinted on the target surface by laser nonuniformities, were varied by using drive with and without SSD. The highest measured neutron-averaged areal densities approach ~150 mg/cm^2, while peak ρR's approach ~180 mg/cm^2 in these implosions. The performances of spherical implosions were correlated with measured target modulations at the end of the acceleration performed in planar target with through-foil radiography. The neutron yield decreases sharply when target modulations become comparable with target thickness (at a target-breakup fraction of about 0.2–0.3). The measured target areal densities are less sensitive to target modulations and slowly decrease when the target-breakup fraction is larger than 0.3.

ACKNOWLEDGMENT

This work was supported by the U.S. Department of Energy Office of Inertial Confinement Fusion under Cooperative Agreement No. DE-FC52-92SF19460, the University of Rochester, and the New York State Energy Research and Development Authority. The support of the DOE does not constitute an endorsement by the DOE of the views expressed in this article.

[1] S. E. Bodner, D. G. Colombant, J. H. Gardner, R. H. Lehmberg, S. P. Obenschain, L. Phillips, A. J. Schmitt, J. D. Sethian, R. L. McCrory, W. Seka, C. P. Verdon, J. P. Knauer, B. B. Afeyan, and H. T. Powell, Phys. Plasmas **5**, 1901 (1998).
[2] J. D. Lindl, Phys. Plasmas **2**, 3933 (1995).
[3] Lord Rayleigh, Proc. London Math. Soc. **XIV**, 170 (1883).
[4] G. Taylor, Proc. R. Soc. London, Ser. A **201**, 192 (1950).
[5] H. Takabe, K. Mima, L. Montierth, and R. L. Morse, Phys. Fluids **28**, 3676 (1985).
[6] R. Betti, V. N. Goncharov, R. L. McCrory, P. Sorotokin, and C. P. Verdon, Phys. Plasmas **3**, 2122 (1996).
[7] K. Shigemori, H. Azechi, M. Nakai, M. Honda, K. Meguro, N. Miyanaga, H. Takabe, and K. Mimi, Phys. Rev. Lett. **78**, 250 (1997).
[8] S. G. Glendinning, S. N. Dixit, B. A. Hammel, D. H. Kalantar, M. H. Key, J. D. Kilkenny, J. P. Knauer, D. M. Pennington, B. A. Remington, R. J. Wallace, and S. V. Weber, Phys. Rev. Lett. **78**, 3318 (1997).
[9] C. J. Pawley, K. Gerber, R. H. Lehmberg, E. A. McLean, A. N. Mostovych, S. P. Obenschain, J. D. Sethian, V. Serlin, J. A. Stamper, C. A. Sullivan, S. E. Bodner, D. Colombant, J. P. Dahlburg, A. J. Schmitt, J. H. Gardner, C. Brown, J. F. Seely, T. Lehecka, Y. Aglitskiy, A. V. Deniz, Y. Chan, N. Metzler, and M. Klapisch, Phys. Plasmas **4**, 1969 (1997).
[10] V. A. Smalyuk, O. Sadot, J. A. Delettrez, D. D. Meyerhofer, S. P. Regan, and T. C. Sangster, Phys. Rev. Lett. **95**, 215001 (2005).
[11] V. A. Smalyuk, V. N. Goncharov, J. A. Delettrez, F. J. Marshall, D. D. Meyerhofer, S. P. Regan, and B. Yaakobi, Phys. Rev. Lett. **87**, 155002 (2001).
[12] M. S. Plesset and T. P. Mitchell, Q. Appl. Math. **13**, 419 (1956).
[13] J. P. Knauer, K. Anderson, R. Betti, T. J. B. Collins, V. Yu. Glebov, V. N. Goncharov, F. J. Marshall, D. D. Meyerhofer, P. B. Radha, S. P. Regan, C. Stoeckl, J. A. Frenje, C. K. Li, R. D. Petrasso, and F. H. Séguin, Bull. Am. Phys. Soc. **50**, 113 (2006).
[14] P. B. Radha, R. Betti, V. Yu. Glebov, V. N. Goncharov, J. P. Knauer, P. W. McKenty, J. A. Marozas, D. D. Meyerhofer, S. P. Regan, T. C. Sangster, and C. Stoeckl, Bull. Am. Phys. Soc. **50**, 113 (2005).
[15] V. N. Goncharov, O. V. Gotchev, E. Vianello, T. R. Boehly, J. P. Knauer, P. W. McKenty, P. B. Radha, S. P. Regan, T. C. Sangster, S. Skupsky, V. A.

Smalyuk, R. Betti, R. L. McCrory, D. D. Meyerhofer, and C. Cherfils-Clérouin, Phys. Plasmas **13**, 012702 (2006).
[16]T. R. Boehly, D. L. Brown, R. S. Craxton, R. L. Keck, J. P. Knauer, J. H. Kelly, T. J. Kessler, S. A. Kumpan, S. J. Loucks, S. A. Letzring, F. J. Marshall, R. L. McCrory, S. F. B. Morse, W. Seka, J. M. Soures, and C. P. Verdon, Opt. Commun. **133**, 495 (1997).
[17]Y. Lin, T. J. Kessler, and G. N. Lawrence, Opt. Lett. **20**, 764 (1995).
[18]T. R. Boehly, V. A. Smalyuk, D. D. Meyerhofer, J. P. Knauer, D. K. Bradley, R. S. Craxton, M. J. Guardalben, S. Skupsky, and T. J. Kessler, J. Appl. Phys. **85**, 3444 (1999).
[19]S. P. Regan, J. A. Marozas, J. H. Kelly, T. R. Boehly, W. R. Donaldson, P. A. Jaanimagi, R. L. Keck, T. J. Kessler, D. D. Meyerhofer, W. Seka, S. Skupsky, and V. A. Smalyuk, J. Opt. Soc. Am. B **17**, 1483 (2000).
[20]J. Delettrez, R. Epstein, M. C. Richardson, P. A. Jaanimagi, and B. L. Henke, Phys. Rev. A **36**, 3926 (1987).